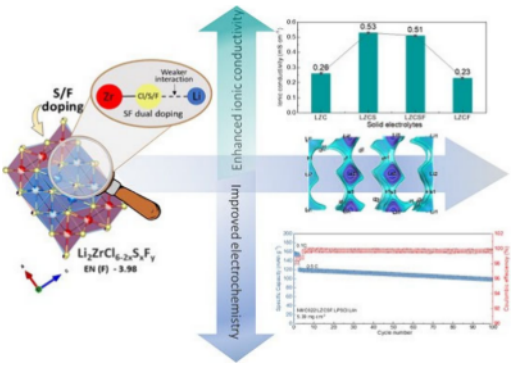
Boosting Ion Transport and Stability in Halide Solid Electrolytes via S and F Codoping

Priya Ganesan, Ramon Zimmermanns, Guillaume Navallon, Yang Hu, Thomas Diemant, Gabriel J. Cuello, Inés Puente Orench, Blanka Detlefs, Ritambhara Gond, Alberto Varzi, Jianneng Liang,* and Maximilian Fichtner*

ABSTRACT: Structural and compositional modification of solid-state electrolytes (SSEs) is a common approach to improve ionic conductivity and interfacial stability, yet the mechanisms remain unclear. Here, we studied Li_2ZrCl_6 (LZC) codoped with sulfur (S) and fluorine (F). X-ray and neutron diffraction with bond valence site energy (BVSE) simulations reveal that codopant-induced lattice distortion facilitates ion transport. The S/F codoped sample achieves a room-temperature ionic conductivity of 0.51 mS cm^{-1}, twice that of pristine LZC (0.26 mS cm^{-1}). Advanced characterizations further show that S and F participate in forming the solid electrolyte interphase (SEI), enhancing the electrode interfacial stability. As a result, solid-state batteries with the codoped SSE deliver capacity retentions of 97.1% at 0.1 C and 82.8% at 0.5 C. This study demonstrates the synergistic effects of structural modulation on ionic conduction and SEI formation, providing insights for designing high-performance SSEs.



All solid-state batteries (ASSBs) are promising energy storage devices due to their potentially high energy density, improved safety, and wider operating temperature range. In this context, oxides, sulfides, and halides are extensively researched as solid-state electrolytes (SSEs).[1−4] However, to meet the requirements of practical applications, the development of an economically viable SSE that combines high ionic conductivity, enhanced voltage stability, and mechanical robustness remains an ongoing challenge.[5,6] Among various systems, Li−M−X materials (Li = lithium; M = metal; X = halogen, typically Cl) have gained attention for their high ionic conductivity (10^{-4}−10^{-2} S cm^{-1}), wide electrochemical stability window (>4 V) compatible with conventional cathodes (unlike sulfide-based SSEs), and favorable mechanical properties. Notable examples include Li_3YCl_6 (LYC), Li_3InCl_6 (LIC), and Li_2ZrCl_6 (LZC), which have been extensively studied as SSEs for lithium batteries.[7−9] Among these, LZC is particularly attractive due to the abundance and cost-effectiveness of Zr, especially when compared to other halide-based SSEs containing yttrium (Y), erbium (Er), and indium (In).[10]

Current research efforts aim to improve the ionic conductivity of SSE and interface stability, often as separate objectives. For the former, structural tuning to exploit structure−property relationships via lattice distortion have been extensively explored.[11−15] For example, Zeier et al. and Nazar et al. have demonstrated that both aliovalent and isovalent doping can significantly enhance ionic conductivity in various halide-based SSE systems.[16−20] To improve interfacial stability, approaches such as doping, artificial coating, and the addition of a liquid-based electrolyte have been explored.[21−23] However, coating techniques require costly instrumentation or precursors. In contrast, doping represents a more economically viable strategy and has been shown to improve electrochemical performance. In particular, fluorine doping is known to enhance interface stability due to its high electronegativity and the formation of a LiF interphase, which is recognized to be electrochemically stable at elevated voltages.[24−28]

In addition, the concept of hybrid doping has been shown to be beneficial due to the redistribution of the anion sites, which induces disorder in the crystal structure and consequently enhances ionic mobility.[29−31] For example, Sn and Se codoping in $Li_{10}GeP_2S_{12}$ (LGPS) has been reported to improve the ionic conductivity by 53% compared to nondoped

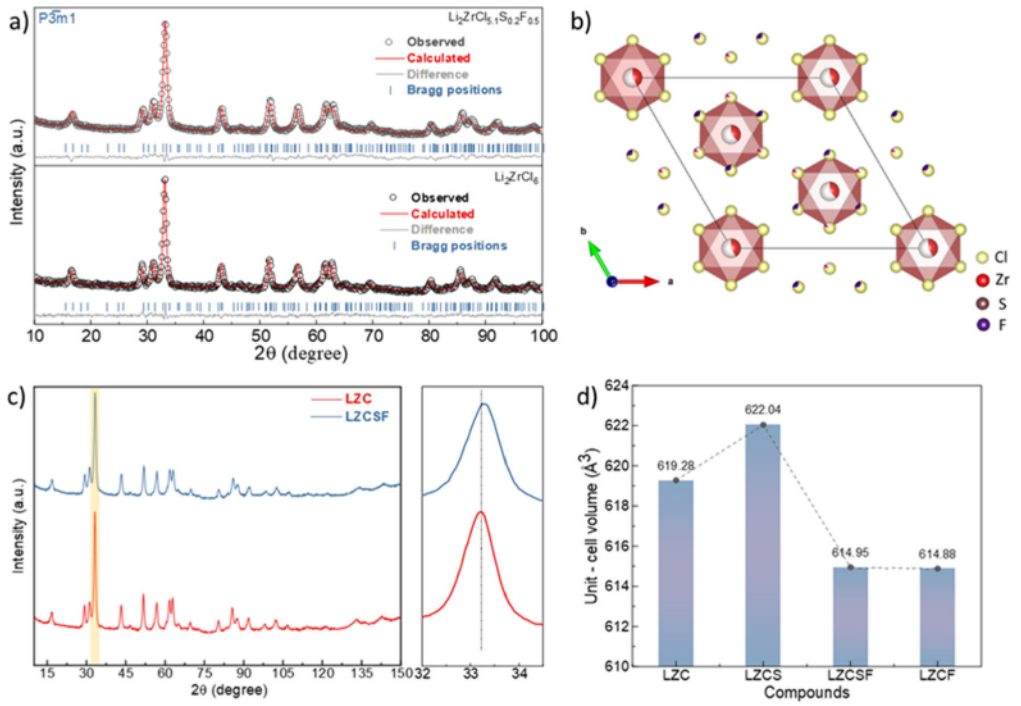


Figure 1. (a) Single-phase Rietveld refinement of $Li_2ZrCl_{5.1}S_{0.2}F_{0.5}$ (LZCSF) and Li_2ZrCl_6 (LZC). (b) Crystal structure of LZCSF with F and S occupying 6i Wyckoff sites corresponding to Cl2 and Cl3 sites. The colors represent chlorine (yellow), zirconium (red), sulfur (brown), fluorine (violet), and vacancies (white). (c) Neutron diffractograms of LZC and LZCSF show a slight shift at 33°, indicative of lattice contraction after S/F substitution. (d) Bar chart illustrating changes in unit cell volume as a function of doping anions (S, F, or SF) obtained from neutron diffraction analysis. The error in the unit cell volumes is less than 1 Å^3.

LGPS.[32] Similarly, iodine and fluorine co-doping in $Li_7P_3S_{11}$ (LPFS) not only facilitates lithium-ion transport but also improves electrochemical stability due to the formation of LiF and LiI at the anode interphase.[33] However, the structure evolution, ionic conductivity, interphase formation mechanisms, and their synergistic effects still need to be explored in enhancing the electrochemical performance of SSBs.

Attracted by the benefits of these strategies, herein, we investigate dual-anion doping of Li_2ZrCl_6 (LZC) SSE with sulfur (S) and fluorine (F). Codoping modifies lattice dynamics, leading to enhanced ionic conductivity and improved interphase stability compared with pristine LZC. The electronegativity of the substituted anions changes bonding interactions and the polarizability of Zr centers, thereby influencing Li^+ diffusion pathways. The S/F codoped $Li_2ZrCl_{5.1}S_{0.2}F_{0.5}$ (LZCSF) exhibits a room-temperature ionic conductivity of 0.51 mS cm^{-1}, more than twice that of pristine LZC (0.26 mS cm^{-1}). Beyond the conductivity, LZCSF also improves the electrochemical stability, achieving capacity retentions of 97.1% and 82.8% at 0.1 and 0.5 C, respectively, at 25 °C with $LiNi_{0.6}Mn_{0.2}Co_{0.2}O_2$ (NMC622) cathodes. Synchrotron X-ray absorption (XAS), X-ray photoelectron spectroscopy (XPS), focused ion beam (FIB), and scanning electron microscopy (SEM) revealed that S and F participate in solid electrolyte interphase (SEI) formation, which stabilizes the NMC622/SSE interface. These findings highlight that careful dopant selection can optimize both ionic conduction and interfacial stability, guiding the development of high-performance SSEs.

Samples with pristine LZC, S-doped LZC (named LZCS), F-doped LZC (named LZCF), and S/F co-doped LZC (named LZCSF) were investigated. The synthesis process of these materials is listed in the Experimental Section in the Supporting Information. To investigate the structural properties of as-synthesized codoped SSE (LZCSF), X-ray diffraction (XRD) using a Ag K_α source (λ = 0.559 Å) was employed. The XRD patterns reveal that the reflections for LZCSF closely match those of undoped LZC, indicating a similar structural framework (Figure S1) with trigonal space group $P\bar{3}m1$ (#164). The reflections of the LZCSF pattern are shifted to the larger angles compared to that of LZC, suggesting lattice contraction, likely attributed to the differing ionic radii of the dopants (S = 1.84 Å, F = 1.33 Å, Cl = 1.81 Å).[34]

Neutron powder diffraction (NPD), neutron pair distribution function (NPDF), and neutron cryo-PDF measurements were performed to obtain more detailed structural insights. Rietveld refinement of the NPD data for LZCSF and LZC is presented in Figure 1a. The refinement for LZCSF yielded a good fit with a χ^2 value of 2.6, confirming the trigonal symmetry. The corresponding diffraction patterns, Rietveld fits, refined lattice parameters, and unit cell volumes are detailed in the Supporting Information (Tables S1 and S2). The neutron diffractograms confirm that LZCSF maintains a crystal structure analogous to that of LZC, comprising alternating Li and Zr layers. Both $Li(Cl/F/S)_6^-$ and $Zr(Cl/F/S)_6^-$ octahedra are present. Rietveld refinement suggests Cl3 site preference for F and Cl2 site preference for S at the 6i Wyckoff positions (Table S2), where 2 and 3 denote the coordinates of chlorine at different *xyz* positions of the respective chlorine atom. The structure is visualized in Figure 1b by VESTA software. Comparison of the neutron diffraction patterns of LZC and LZCSF reveals a slight shift in all of the reflections to higher 2θ for LZCSF, consistent with the XRD results. For example, Figure 1c shows one of the reflections at 33° exhibiting a right shift in LZCSF in comparison to LZC. To evaluate the impact of doping on the unit cell volume,

neutron diffraction data were collected for LZCF and LZCS under identical conditions. The results are summarized in Figure 1d, showing the following trend: LZCS (622 ± 1 Å^3) > LZC (619 ± 1 Å^3) > LZCSF (614 ± 1 Å^3) > LZCF (614 ± 1 Å^3). This trend highlights the significant influence of electronegativity (S = 2.58 Å < Cl = 3.16 Å < F = 3.98 Å) and ionic radii of the dopants on lattice distortion. The observed contraction or expansion supports the successful incorporation of dopants at chlorine sites. Single-phase Rietveld refinement was also successfully performed for LZC and LZCSF assuming a trigonal structure ($P\bar{3}m1$). For LZCF and LZCS, the detailed refinement results have been shown in our previous work.[35,36]

Neutron cryo- PDF measurements were carried out for LZC and LZCSF. These were recorded at a temperature of 10 K, which minimizes thermal vibrations and allows for more accurate structural insight. From the cryo-PDF data, the polyhedral volumes of Zr and Li octahedra were calculated. The structural refinement details are provided in the Supporting Information in Tables S3 and S4.

Room-temperature PDFs (Figure S2) for all four compositions (LZC, LZCS, LZCF, and LZCSF) display broadly similar profiles, suggesting that the average local structure remains largely unchanged upon doping. The first peak (~2.460 ± 0.003 Å) corresponds to Zr−Cl bond length. The second peak (3.57 Å), attributed to Cl−Cl distances within the octahedra, shows notable asymmetry, likely due to the presence of two distinct octahedral types: $Li(Cl/F/S)_6^-$ and $Zr(Cl/F/S)_6^{2-}$. Although these units are similar in size, their different local environment results in overlapping but nonidentical contributions, producing a single asymmetric peak. The neutron PDFs of LZC and LZCSF are dominated by Cl correlations due to the comparatively large scattering length and high abundancy of Cl in the material. F and S pairs are not directly detected; thus, only their influence on the Cl bond lengths can be interpreted; the same is true for Li.

The results reveal that the Zr−Cl bond length increases upon fluorine doping, while the Li octahedra compensate via an opposing distortion, maintaining the overall structural balance. This is evident from the contrasting shifts in the first and second peaks in cryo-PDFs of LZCSF compared to LZC (Figure 2a). The second peak is less asymmetric in the codoped sample and shifts to shorter distances. As expected, cryo-PDFs exhibit sharper peaks and more distinct features due to reduced thermal vibrations (the corresponding fits are shown in Figure S3). Nevertheless, distinct Li correlations are not clearly resolved owing to the overlap with Zr and Cl peaks and the low scattering length of Li. Interestingly, peaks in the LZCSF PDF are broader than in LZC, suggesting a higher degree of disorder in the codoped structure.

Variations in Zr−Cl bond lengths are likely governed by the polarizability and electronegativity of the dopant anions. Sulfur, with the lowest electronegativity and highest polarizability among S^{2-}, Cl^-, and F^-, forms weaker bonds with Zr due to its larger size. This leads to increased electron density around the Zr ion, effectively strengthening Zr−Cl bonds and shortening them slightly. Moreover, replacing Cl^- by S^{2-} introduces vacancies in the Cl sublattice to maintain charge neutrality, further altering the local structure. In contrast, fluorine, with the highest electronegativity and lowest polarizability, draws electron density away from Zr, resulting in weakened Zr−Cl bonds and slightly longer bond lengths. Interestingly, Zr bonds with the dopants (S and F) behave in

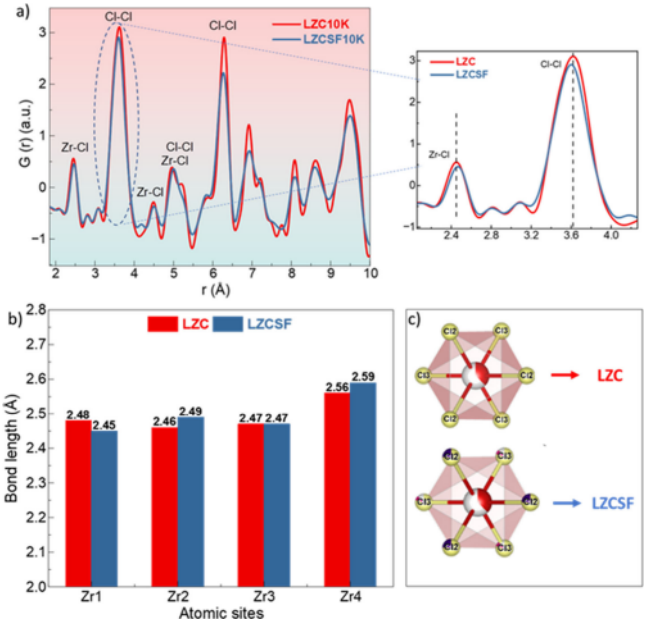


Figure 2. (a) Neutron pair distribution functions, $\mathfrak{G}(r)$, of LZC (red) and LZCSF (blue), with the inset highlighting shifts in bond lengths. The region at r > 5 Å corresponds to Cl−Cl distances in the next coordination shell. Comparison of the bond lengths of (b) zirconium sites of LZC and LZCSF, along with the (c) VESTA images of Zr octahedra following sulfur and fluorine co-doping. The crystallographically distinct zirconium atoms located at unique atomic positions (x, y, z) in the crystal lattice are denoted with the numbers 1−4 for zirconium as Zr1, Zr2, Zr3, and Zr4. The zirconium atom is presented in red, chlorine in yellow, fluorine in violet, sulfur in brown, and vacancies in white.

opposite ways, balancing the distortions produced by each dopant. The change in bond length at unique zirconia atomic sites are presented as a bar diagram in Figure 2b, with the structural representation of one of the zirconium octahedra for both LZC and LZCSF in Figure 2c. Compared to Zr3, the Zr1, Zr2, and Zr4 sites are more affected by the incorporation of sulfur and fluorine, which further confirms the probability of substitution of the dopants in the lattice. The zirconium and lithium polyhedral volume changes are presented in Figure S4a,b.

LZCSF shows an average increase in polyhedral volume with decreasing unit cell volume by S and F substitution (Figure 1d), demonstrating an inverse relationship between polyhedral volume and unit cell volume. This is likely explained by octahedral distortions due to substitution effects governed by the differences in the ionic radii of the dopants (F < Cl). This is structurally visualized in Figure S4c−f showing the distortion of the octahedra for LZCSF, whereas for LZC no such distortions were seen. This phenomenon has been previously reported for perovskite systems such as $NaMgF_3$ and ReO_3-type perovskites.[37−41] Hence, from neutron diffraction and PDF analysis, the incorporation of S and F in the structure is confirmed. Additionally, scanning electron microscopy (SEM) coupled with energy dispersive X-ray (EDX) studies show irregular agglomerated SSE particles with homogeneous distribution of sulfur and/or fluorine across all samples (Figure S5).

The ionic conductivity values of LZC, LZCS, LZCF, and LZCSF at 25 °C are 0.26, 0.53, 0.51, and 0.23 mS cm^{-1} for LZC, LZCS, LZCSF, and LZCF, respectively (Figure 3a). The

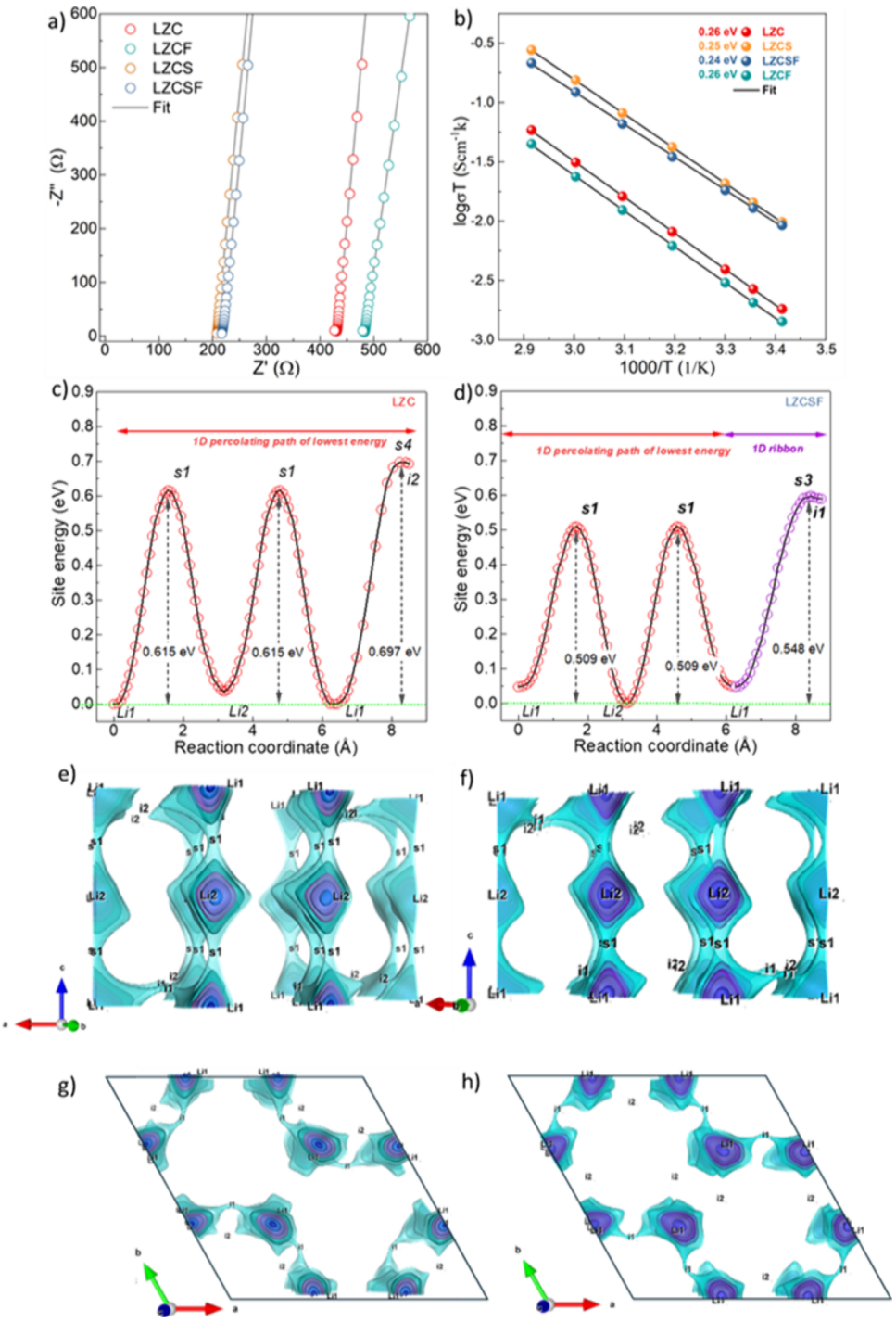


Figure 3. (a) Nyquist plots of LZC, LZCS, LZCF, and LZCSF recorded at 25 °C. (b) Arrhenius plots showing log (σT) vs 1000/T over the temperature range 293−343 K. Energy profiles calculated from BVSE for (c) LZC and (d) LZCSF. Corresponding ribbon structures in ac and ab plane of (e and g) LZC and (f and h) LZCSF.

ionic conductivity values follow the trend of LZCS > LZCSF > LZC > LZCF, consistent with the electronegativity of dopant anions. The electronegativities of dopants play critical roles in determining the conductivity mechanism of SSEs. Substituting highly electronegative atoms, such as fluorine (EN = 3.98), weakens the Zr−Cl bonds while strengthening Cl−Li interactions, thereby increasing the migration energy barrier of Li^+ ions. In contrast, substituting a low electronegative atom S^{2-} (EN = 2.58) in chlorine site not only weakens the interaction but also introduces vacancies in the anion sublattice, potentially promoting lithium ion diffusion.[42,43] The nature of the anion framework plays a key role in determining the size of transport channels and thus modulating the diffusion pathways.[44] Combining both S and F, as in LZCSF, leads to enhanced ionic conductivity and reduced activation energy compared to the undoped LZC. The trend in activation energy is LZCSF (0.24 eV) > LZCS (0.25 eV) > LZC (0.26 eV) > LZCF (0.26 eV), indicating that LZCS exhibits the best overall ionic conducting performance (Figure 3b). The corresponding Nyquist plots at different temperatures

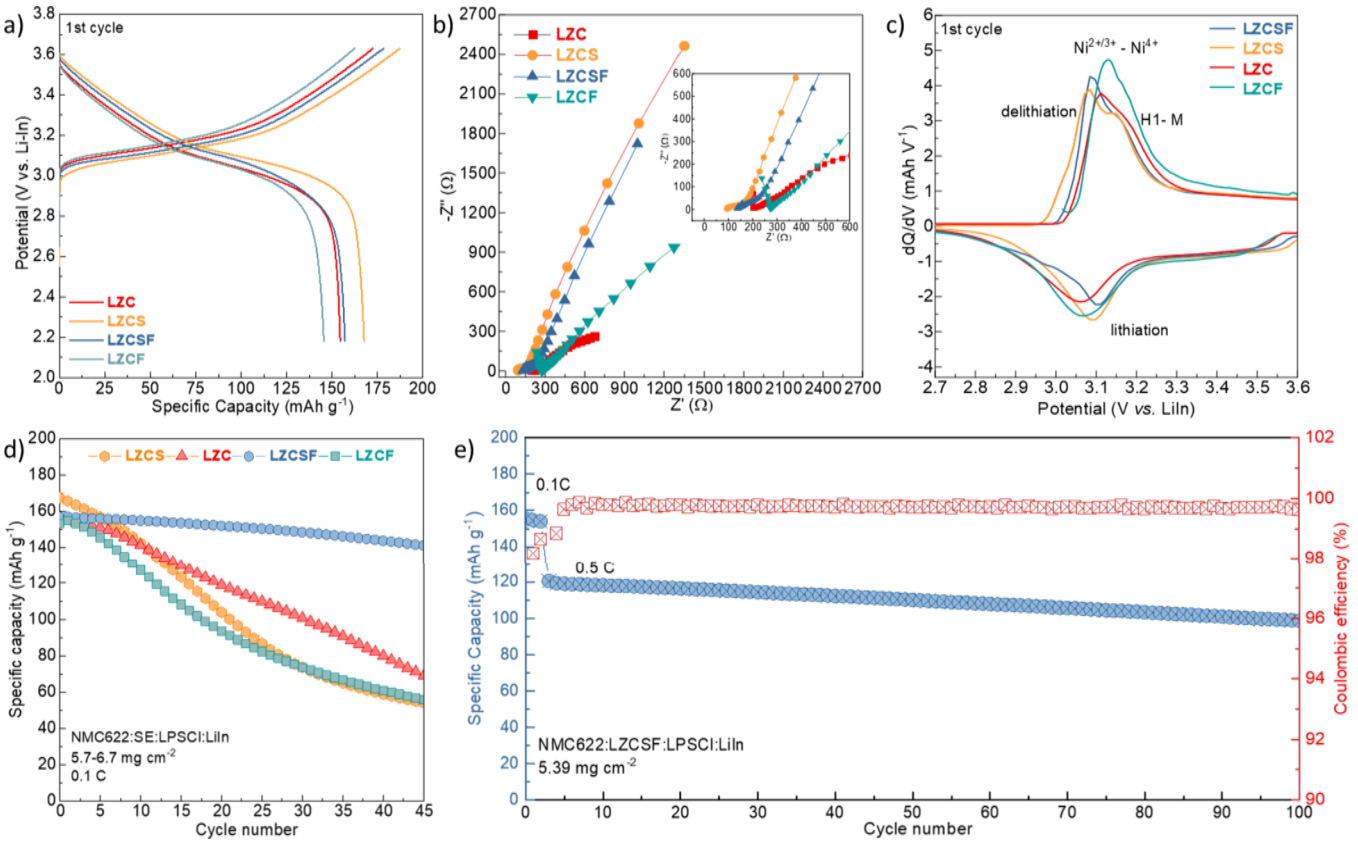


Figure 4. Galvanostatic electrochemical performance of LZC, LZCS, LZCSF and LZCF at 25 °C. (a) Initial charge−discharge profiles for all systems at 0.1 C. (b) Nyquist plots were obtained immediately after cell assembly. (c) Differential capacity (dQ/dV) plots highlighting lithiation and delithiation behavior. (d) Comparison of discharge capacities at 0.1 C with an active material mass loading of 5−6 mg cm^{-2}. (e) Cycling performance of LZCSF at 0.5 C, showing a stable capacity of 120 mA h g^{-1} after 100 cycles at room temperature.

and electronic conductivity values for all four compositions are shown in Figures S6 and S7. The electronic conductivity values are in the range of 10^{-10} to 10^{-11} S·cm^{-1}, i.e., 6 orders of magnitude lower than their ionic conductivities. This confirms that these materials behave as ideal SSEs with negligible electronic conduction. These values were calculated using eqs 1 and 2 in the Supporting Information.

To further understand Li^+ transport behavior and potential diffusion pathways, bond-valence site energy (BVSE) calculations were performed as previously reported,[45−47] using a two-body Morse-type force field based on the bond-valence model (Figure 3c−f). In both LZC and LZCSF, Li^+ hopping occurs along the *c*-axis, starting from Li1 (LZC) and Li2 (LZCSF) sites and passing through saddle point s1, with migration barriers of 0.614 and 0.509 eV, respectively. The lowest-energy pathways are Li1−s1−Li2 for LZC and Li2−s1−Li1 for LZCSF (Figure 3c,d). Superimposed ribbon-like structures illustrating these pathways are shown in Figure 3e−h. When the three-dimensional isosurfaces are viewed along the ac plane (Figure 3e,f), the conduction channels in LZC and LZCSF appear to be similar. However, the ab plane projections (Figure 3g,h) reveal subtle but important differences in the distribution of favorable interstitial sites. These results align with PDF analysis, indicating that S^{2-}/F^- codoping modifies bond distances and local environments, facilitating Li^+ diffusion with reduced migration barriers compared to the undoped structure. It should be noted that the activation energies predicted by BVSE are higher compared to experimental values because BVSE does not account for nonperiodic features such as internal strains, particle size variations that are introduced by mechanochemical milling.[48,49]

Figure 4 provides a comparative overview of the electrochemical performances of solid-state batteries (SSBs), including SSEs with different dopants. The first cycle charge−discharge profiles in Figure 4a show that LZCS exhibited the highest initial discharge capacity of 175 mA h g^{-1}, followed by LZC and LZCSF at 150 mA h g^{-1} and LZCF at 145 mA h g^{-1}. This trend is consistent with the ionic conductivity order: LZCS > LZCSF > LZC > LZCF. The initial high capacity of LZCS can be attributed to the enhanced Li^+ diffusion by sulfur doping, which promotes higher ionic conductivity, thereby facilitating efficient lithiation of NMC 622. In contrast, the strong Li−F interactions in the highly electronegative fluorine-doped LZCF restrict Li^+ mobility, resulting in a reduced initial capacity. This relationship is further supported by the Nyquist plot shown in Figure 4b, where the resistance values for LZC, LZCS, LZCSF, and LZCF are 205.6, 95.1, 136.8, and 272.7 Ω, respectively, mirroring the discharge capacity trend. The differential capacity (dQ/dV) plots shown in Figure 4c provide insights into the structural transformations occurring during the first charge−discharge cycle. Two distinct oxidation peaks are clearly evident at around 3.1 and 3.2 V during delithiation, corresponding to phase transitions between hexagonal phases (H1 → H2). An additional shoulder peak during oxidation indicates further phase transitions, notably H1 → M.[50] A reversible lithiation peak at lower potentials due to increased polarization is

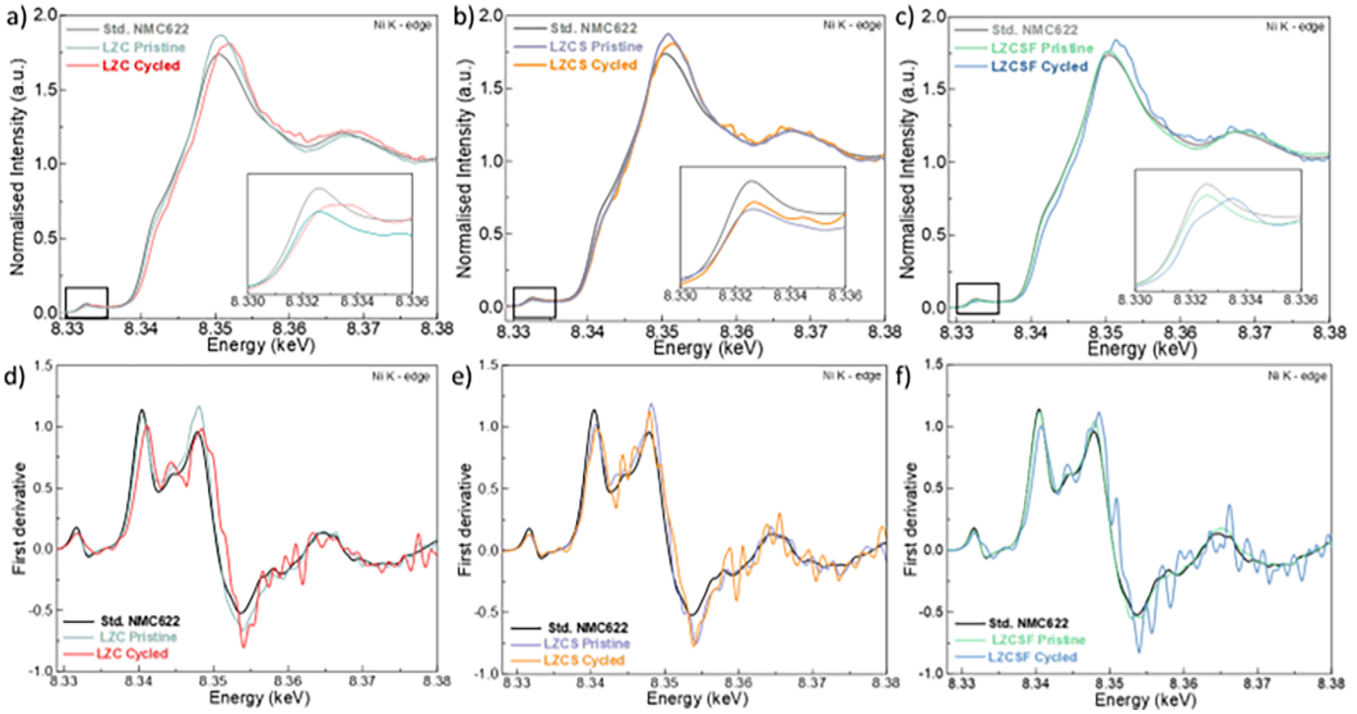


Figure 5. Ni K-edge X-ray absorption spectra (XAS) with the inset depicting pre-edge features of (a) LZC, (b) LZCS, and (c) LZCSF with the respective first-derivative plots for (d) LZC, (e) LZCS, and (f) LZCSF, before and after cycling.

observed. Figure 4d compares the cycling stability of the systems at 0.1C. After 45 cycles, LZC, LZCS, and LZCF displayed similar capacity fading, while LZCSF maintained a discharge capacity of 150 mA hg^{-1}. The corresponding capacity retention values were 78% for LZC, 64% for LZCS, 70% for LZCF, and 98% for LZCSF. The superior retention of LZCSF (Figure S8a) is attributed to the combined benefits of fluorine incorporation, which is known to enhance electrochemical performance via Li−F bond formation,[51] and its enhanced ionic conductivity compared to LZC and LZCF. Although sulfur-doped systems demonstrate higher conductivity, their narrow oxidative stability window and potential formation of sulfates or sulfoxides may limit long-term performance. Therefore, the dual-doping strategy in LZCSF likely contributes to its improved ionic conductivity and enhanced oxidative stability. To further probe the long-term stability of LZCSF, cycling was performed at 0.5 C (Figure 4e). After 100 cycles, the system retained ca. 83% of its initial capacity, delivering 120 mA hg^{-1} (Figure S8b). To evaluate the roles of dopants at high rate performance, rate capability tests were performed from 0.1 to 1 C for LZCS and LZCSF (see Figure S8). At 1 C, LZCSF delivered 58.5 mA h g^{-1} capacity outperforming LZCS (33.5 mAh g^{-1}) after 35 cycles, highlighting the impact of S/F codoping.

To probe interphase compounds, XPS measurements were carried out on NMC-SSE composite electrodes at different stages of cycling (i.e., pristine electrode, first discharged, and 10^{th} discharged state). The F 1s spectra (Figure S9a) show a minor shift from 685.1 to 685.2 eV with peak broadening after cycling (FWHM: Pristine -1.63 eV, cycled -1.75 eV), which could indicate the formation of LiF due to the presence of F dopant for LZCSF SSE. However, a definitive verification is difficult due to overlapping binding energies of LiF (typically at 685.0−685.5 eV) and LZCSF. For the S 2p spectra (Figure S9b), similar to the parent compound LZCS,[36] a single peak doublet (S $2p_{3/2}$ peak at 161.4 eV) was observed for pristine LZCSF powder. The lack of a chemical shift between LZCS and LZCSF points to rather small changes of the electronic structure of sulfur by fluorine insertion. Surprisingly, the picture changed completely after intermixing LZCSF with NMC and carbon black (CB) and preparation of the pristine NMC−SSE composite electrode. In fact, while the initial peak doublet was still detected (with lower intensity), a new peak doublet at higher binding energy (S $2p_{3/2}$ peak at 163.5 eV) dominated the S 2p spectrum. Usually, a peak doublet at this binding energy can be attributed to (internal) S atoms of polysulfides.[52,53] In addition, another peak doublet due to sulfate is observed at even higher binding energy (S $2p_{3/2}$ peak at 169.2 eV). Since the electrode preparation was carried out under inert gas and without any solvent, the result points to reaction of LZCSF SSE with NMC (or CB) during the electrode preparation, forming polysulfides and sulfate interphase materials. Further details are provided in the Supporting Information. The spectra of cycled electrodes (1^{st}discharged and 10^{th} discharged state) exhibited relatively small changes from that of the pristine electrode; while the intensity of the doublet at the lowest binding energy decreases slightly, as the sulfate signal grows (Figure S9b,c). The formation of sulfate and fluorine species suggests the possible presence of fluorosulfonate compounds which have been reported to enhance electrochemical performance.[54] Further investigation using advanced techniques such as TOF-SIMS is necessary to identify the buried interphase products. However, this is beyond the scope of the current work. The XPS results suggest that with S−F co-doping, a fluorine-rich interphase is formed at the interface. This could be the reason for the improved interface stability. Finally, the Zr 3d and Cl 2p spectra remained unchanged in all stages of cycling (Figures S10−S12).

To further investigate the interface stability between SSEs and NMC622 active material, HERFD-XAS spectra of Ni, Mn, and Co K-edge were measured to reveal possible differences in the electronic structure of NMC transition metal in the presence of the SSEs, before and after 20 cycles. Figure 5a–c shows the Ni K-edge absorption spectra of electrodes in their pristine and discharged states after 20 cycles. Bare NMC622 powder was used as a standard, here represented by the black curve. Ni K-edge spectra show an obvious increase in the energy of the edge after 20 cycles for electrodes prepared with LZC and LZCSF, but not LZCS. This shift to higher energy suggests partial retention of a higher degree of oxidation of Ni after several cycles. This behavior has already been reported in previous work on Ni-rich NMC.[55] Electrodes prepared with LZCS do not exhibit such a shift of the edge position as made visible in Figure 5d–f representing the first derivative of the K-alpha emission intensity. In addition to the edge shift, the pre-edge shape was also largely affected for electrodes containing LZC and LZCSF but not for LZCS. This change of shape and higher intensity arise from distortion of the Ni sites and mixing of the 3d/4p orbitals.[56,57] We attribute the unchanged spectra of LZCS electrodes to SSE degradation, as confirmed by the XPS analysis where the presence of polysulfides and sulfates in cycled electrodes has been identified. Degradation products of the SSE disrupt Li^+ conduction and limit NMC redox activity, explaining the preserved Ni oxidation state and rapid capacity loss.

Mn K-edge absorption spectra (Figure S13) show no change in edge or pre-edge features after cycling for any of the three electrolytes, consistent with previous reports that the Mn oxidation state in NMC remains constant during cycling.[58] The origin of the systematic shift between the NMC standard and the pristine electrode is discussed in the Supporting Information. Co K-edge spectra (Figure S14) show no edge shift after cycling, indicating the preserved Co oxidation states. However, the pre-edge intensity increases for cycled LZC and LZCS electrodes, suggesting local Co environment distortion. This change is absent in LZCSF electrodes, supporting their more stable cycling behavior.

SEM images of FIB-milled NMC622-SSE interfaces (Figure S15) and EDX line scans revealed the interfacial diffusion of oxygen and nickel in both LZC and LZCSF. LZCSF showed significantly shorter diffusion distances than undoped LZC, indicating improved interfacial stability and reduced transition metal migration. S and F substitutions likely suppress interfacial degradation and mitigates mechanical stress, preserving NMC particle integrity during cycling.[59−62]

In summary, this work reports a S/F co-doped Li_2ZrCl_6 SSE (LZCSF), where dual-anion substitution modifies the lattice, enhancing ionic conductivity and promoting S/F participation in SEI formation, improving interfacial stability. Co-doping induces lattice contraction for LZCSF and expansion for LZCS, tuning the unit cell volumes. BVSE calculations show enhanced Li^+ diffusion. Although its conductivity (0.51 mS cm^{-1}) is slightly lower than that of LZCS (0.54 mS cm^{-1}), dual-anion incorporation boosts electrochemical performance. SSB with LZCSF retains 83% capacity at 0.5 C after 100 cycles, delivering 110 mAh g^{-1}. XPS shows LiF and sulfate formation at the interphase, and synchrotron XAS reveals a more reversible Ni oxidation state after cycling. FIB-EDX scans indicate a thinner interphase in LZCSF versus LZC. This co-doping strategy enhances both ionic conductivity and electrochemical stability, highlighting the need to balance these properties in halide SSEs and offering a promising approach for the rational design of next-generation SSEs.

AUTHOR INFORMATION

Corresponding Authors

Jianneng Liang − *Helmholtz Institute Ulm (HIU) Electrochemical Energy Storage, 89081 Ulm, Germany; Karlsruhe Institute of Technology (KIT), 76021 Karlsruhe, Germany;* orcid.org/0000-0001-7000-7820; Email: jianneng.liang@kit.edu

Maximilian Fichtner − *Helmholtz Institute Ulm (HIU) Electrochemical Energy Storage, 89081 Ulm, Germany; Karlsruhe Institute of Technology (KIT), 76021 Karlsruhe, Germany;* orcid.org/0000-0002-7127-1823; Email: m.fichtner@kit.edu

Authors

Priya Ganesan − *Helmholtz Institute Ulm (HIU) Electrochemical Energy Storage, 89081 Ulm, Germany; Karlsruhe Institute of Technology (KIT), 76021 Karlsruhe, Germany*

Ramon Zimmermanns − *Helmholtz Institute Ulm (HIU) Electrochemical Energy Storage, 89081 Ulm, Germany; Karlsruhe Institute of Technology (KIT), 76021 Karlsruhe, Germany*

Guillaume Navallon − *Helmholtz Institute Ulm (HIU) Electrochemical Energy Storage, 89081 Ulm, Germany; Karlsruhe Institute of Technology (KIT), 76021 Karlsruhe, Germany;* orcid.org/0009-0005-8005-0204

Yang Hu − *Helmholtz Institute Ulm (HIU) Electrochemical Energy Storage, 89081 Ulm, Germany; Karlsruhe Institute of Technology (KIT), 76021 Karlsruhe, Germany;* orcid.org/0000-0001-6864-6498

Thomas Diemant − *Helmholtz Institute Ulm (HIU) Electrochemical Energy Storage, 89081 Ulm, Germany; Karlsruhe Institute of Technology (KIT), 76021 Karlsruhe, Germany*

Gabriel J. Cuello − *Institut Laue-Langevin, 38042 Grenoble, France*

Inés Puente Orench − *Institut Laue-Langevin, 38042 Grenoble, France*

Blanka Detlefs − *European Synchrotron Radiation Facility, 38000 Grenoble, France;* orcid.org/0000-0002-9768-647X
Ritambhara Gond − *Department of Electrical Engineering, Chalmers University of Technology, 41296 Göteborg, Sweden*
Alberto Varzi − *Helmholtz Institute Ulm (HIU) Electrochemical Energy Storage, 89081 Ulm, Germany; Karlsruhe Institute of Technology (KIT), 76021 Karlsruhe, Germany;* orcid.org/0000-0001-5069-0589

Author Contributions

P.G. and J.L. conceptualized the work. P.G. designed and carried out the structural and electrochemical experiments, XANES, NPD, NPDF, analyzed, discussed the data, and wrote the manuscript. M.F. supervised the work, discussed the data, corrected the manuscript, and provided funding. J.L. and A.V. supervised and discussed the data. R.Z. carried out NPDF analysis and refinement and discussed the data. G.J.C. and I.P.O carried out neutron diffraction experiments and helped with the analysis. Y.H. performed NPD and NPDF and helped with the analysis of XANES measurements. G.N. and B.D carried out XAS measurements and the data analysis. T.D. performed the XPS experiments. R.G performed the BVSE calculations and the analysis. All authors reviewed the final version of the manuscript.

Notes

The authors declare no competing financial interest.

■ ACKNOWLEDGMENTS

This work contributes to the research performed at CELEST (Center for Electrochemical Energy Storage Ulm-Karlsruhe) and was partly funded by the German Research Foundation (DFG) under Project ID 390874152 (POLiS Cluster of Excellence). We thank the Institut Laue-Langevin (ILL) for the provision of beamtime at D2B and D4 beamlines under the proposal 6-06-536 (data at DOI: 10.5291/ILL-DATA.6-06-536). We are also grateful for the utilization of ID26 beamline at The European Synchrotron Radiation Facility (ESRF) under the HUB proposal MA6230 (Data: 10.15151/ESRF-ES-1901542598). J.L. and A.V. acknowledge financial support from the Federal Ministry for Economic Affairs and Energy (BMWE) in the frame of the REFA (03EI6055B) and ELIC (03ETE034C) projects, as well as the Helmholtz Association.

■ REFERENCES

(1) Famprikis, T.; Canepa, P.; Dawson, J. A.; Islam, M. S.; Masquelier, C. Fundamentals of Inorganic Solid-State Electrolytes for Batteries. *Nat. Mater.* **2019**, *18* (12), 1278−1291.
(2) Yu, T.; Liu, Y.; Li, H.; Sun, Y.; Guo, S.; Zhou, H. Ductile Inorganic Solid Electrolytes for All-Solid-State Lithium Batteries. *Chem. Rev.* **2025**, *125* (6), 3595−3662.
(3) Li, X.; Kim, J. T.; Luo, J.; Zhao, C.; Xu, Y.; Mei, T.; Li, R.; Liang, J.; Sun, X. Structural Regulation of Halide Superionic Conductors for All-Solid-State Lithium Batteries. *Nat. Commun.* **2024**, *15* (1), 1−8.
(4) Liang, J.; Luo, J.; Sun, Q.; Yang, X.; Li, R.; Sun, X. Recent Progress on Solid-State Hybrid Electrolytes for Solid-State Lithium Batteries. *Energy Storage Mater.* **2019**, *21* (May), 308−334.
(5) Wang, S.; La Monaca, A.; Demopoulos, G. P. Composite Solid-State Electrolytes for All Solid-State Lithium Batteries: Progress. *Challenges and Outlook. Energy Adv.* **2025**, *4* (1), 11−16.
(6) Lee, D.; Kumar Kakarla, A.; Sun, S.; Joohyun Kim, P.; Choi, J. Inorganic Solid-State Electrolytes for Solid-State Sodium Batteries: Electrolyte Design and Interfacial Challenges. *ChemElectroChem.* **2025**, *12*, No. e202400612.
(7) Li, C.; Du, Y. Building a Better All-Solid-State Lithium-Ion Battery with Halide Solid-State Electrolyte. *ACS Nano* **2025**, *19* (4), 4121−4155.
(8) Zhang, Y.; Sun, J.; Li, L.; Long, Z.; Meng, P.; Ang, E. H.; Liang, Q. Advancements in the Emerging Rare-Earth Halide Solid Electrolytes for next-Generation All-Solid-State Lithium Batteries. *Coord. Chem. Rev.* **2025**, *528* (December 2024), No. 216432.
(9) Li, X.; Liang, J.; Chen, N.; Luo, J.; Adair, K. R.; Wang, C.; Banis, M. N.; Sham, T. K.; Zhang, L.; Zhao, S.; Lu, S.; Huang, H.; Li, R.; Sun, X. Water-Mediated Synthesis of a Superionic Halide Solid Electrolyte. *Angew. Chemie - Int. Ed.* **2019**, *58* (46), 16427−16432.
(10) Wang, K.; Ren, Q.; Gu, Z.; Duan, C.; Wang, J.; Zhu, F.; Fu, Y.; Hao, J.; Zhu, J.; He, L.; Wang, C. W.; Lu, Y.; Ma, J.; Ma, C. A Cost-Effective and Humidity-Tolerant Chloride Solid Electrolyte for Lithium Batteries. *Nat. Commun.* **2021**, *12* (1), 4410.
(11) Deng, M.; Liu, S.; Li, S.; Hu, W.; Lu, Z.; Jiang, Z.; Li, L.; Tang, K.; Shi, L.; Luo, Q.; Li, H.; Yang, J.; Liu, C.; Yu, C. Recovering the Ionic Conductivity of Oxygen-Doped Li3.25InCl5.75O0.25 Electrolyte through Heat Treatment: Reconstructing the Structure Damaged by Moisture. *ChemSusChem* **2025**, *18* (14), No. e202500495.
(12) Luo, Q.; Ming, L.; Zhang, D.; Wei, C.; Wu, Z.; Jiang, Z.; Liu, C.; Liu, S.; Cao, K.; Zhang, L.; Yu, C.; Cheng, S. Constructing Br-Doped Li10SnP2S12-Based All-Solid-State Batteries with Superior Performances. *Energy Mater. Adv.* **2023**, *4*, 1−12.
(13) Chen, S.; Yu, C.; Wei, C.; Jiang, Z.; Zhang, Z.; Peng, L.; Cheng, S.; Xie, J. Unraveling Electrochemical Stability and Reversible Redox of Y-Doped Li2ZrCl6 Solid Electrolytes. *Energy Mater. Adv.* **2023**, *4*, 4−13.
(14) Deng, M.; Li, S.; Jiang, Z.; Li, L.; Lu, Z.; Liu, S.; et al. A Zr−O Co-Doping Strategy for Halide Solid Electrolytes toward High-Performance All-Solid-State Batteries. *J. Mater. Chem. A* **2025**, *13*, 32471−32480.
(15) Chen, S.; Yu, C.; Chen, S.; Peng, L.; Liao, C.; Wei, C.; Wu, Z.; Cheng, S.; Xie, J. Enabling Ultrafast Lithium-Ion Conductivity of Li2ZrCl6 by Indium Doping. *Chin. Chem. Lett.* **2022**, *33* (10), 4635−4639.
(16) Martinez de Irujo-Labalde, X.; Zhao, T.; Samanta, B.; Bernges, T.; Faka, V.; Sobolev, A. N.; Maus, O.; Appel, M.; Kraft, M. A.; Hansen, M. R.; Zeier, W. G. How Crystal Structure and Microstructure Can Influence the Sodium-Ion Conductivity in Halide Perovskites. *J. Mater. Chem. A* **2024**, *12* (1), 33707−33722.
(17) Banik, A.; Samanta, B.; Helm, B.; Kraft, M. A.; Rudel, Y.; Li, C.; Hansen, M. R.; Lotsch, B. V.; Bette, S.; Zeier, W. G. Exploring Layered Disorder in Lithium-Ion-Conducting Li3Y1-XInxCl6. *Inorg. Chem.* **2024**, *63* (19), 8698−8709.
(18) Zhou, L.; Zuo, T.; Li, C.; Zhang, Q.; Janek, J.; Nazar, L. F. Li3-XZrx(Ho/Lu)1-XCl6 Solid Electrolytes Enable Ultrahigh-Loading Solid-State Batteries with a Prelithiated Si Anode. *ACS Energy Lett.* **2023**, *8* (7), 3102−3111.
(19) Zhou, L.; Zuo, T. T.; Kwok, C. Y.; Kim, S. Y.; Assoud, A.; Zhang, Q.; Janek, J.; Nazar, L. F. High Areal Capacity, Long Cycle Life 4 V Ceramic All-Solid-State Li-Ion Batteries Enabled by Chloride Solid Electrolytes. *Nat. Energy* **2022**, *7* (1), 83−93.
(20) Liu, Z.; Chien, P. H.; Wang, S.; Song, S.; Lu, M.; Chen, S.; Xia, S.; Liu, J.; Mo, Y.; Chen, H. Tuning Collective Anion Motion Enables Superionic Conductivity in Solid-State Halide Electrolytes. *Nat. Chem.* **2024**, *16*, 1584−1591.
(21) Lyu, S.; Yu, J.; Guo, X. H.; Bu, X.; Sun, L.; Li, N.; Chen, H.-S.; Song, W. L.; Yu, X.; Jiao, S. Mechanistically Understanding the Correlation Between Dynamic Interface Variation and Stability of Surface Coating on the NMC811 Materials. *Adv. Energy Mater.* **2025**, *2403270*, 2403270.
(22) Liu, Q.; Chen, Q.; Tang, Y.; Cheng, H. M. Interfacial Modification, Electrode/Solid-Electrolyte Engineering, and Monolithic Construction of Solid-State Batteries*Electrochem. Energy Rev.*615. 2023 DOI: 10.1007/s41918-022-00167-1

(23) Wei, L.; Li, L.; Zhao, T.; Zhang, N.; Zhao, Y.; Wu, F.; Chen, R. MOF-Derived Lithiophilic CuO Nanorod Arrays for Stable Lithium Metal Anodes. *Nanoscale* **2020**, *12*, 9416−9422.
(24) Yu, T.; Liang, J.; Luo, L.; Wang, L.; Zhao, F.; Xu, G.; Bai, X.; Yang, R.; Zhao, S.; Wang, J.; Yu, J.; Sun, X. Superionic Fluorinated Halide Solid Electrolytes for Highly Stable Li-Metal in All-Solid-State Li Batteries. *Adv. Energy Mater.* **2021**, *11* (36), 2101915.
(25) Wang, Q.; Ma, X.; Liu, Q.; Sun, D.; Zhou, X. Fluorine-Doped Li3InCl6 to Enhance Ionic Conductivity and Air Stability. *J. Alloys Compd.* **2023**, *969* (August), No. 172479.
(26) Xu, X.; Du, G.; Cui, C.; Liang, J.; Zeng, C.; Wang, S.; Ma, Y.; Li, H. Stabilizing the Halide Solid Electrolyte to Lithium by a β-Li3N Interfacial Layer. *ACS Appl. Mater. Interfaces* **2022**, *14* (35), 39951−39958.
(27) Yan, H.; Yao, J.; Ye, Z.; Lin, Q.; Zhang, Z.; Li, S.; Song, D.; Wang, Z.; Yu, C.; Zhang, L. Al-F Co-Doping towards Enhanced Electrolyte-Electrodes Interface Properties for Halide and Sulfide Solid Electrolytes. *Chin. Chem. Lett.* **2025**, *36* (1), No. 109568.
(28) Akkinepally, B.; Reddy, I. N.; Ko, T. J.; Yoo, K.; Shim, J. Dopant Effect on Li+ Ion Transport in NASICON-Type Solid Electrolyte: Insights from Molecular Dynamics Simulations and Experiments. *Ceram. Int.* **2022**, *48* (9), 12142−12151.
(29) Yu, P.; Ahmad, N.; Yang, J.; Zeng, C.; Liang, X.; Huang, W.; Ni, M.; Mao, P.; Yang, W. Dual-Doping for Enhancing Chemical Stability of Functional Anionic Units in Sulfide for High-Performance All-Solid-State Lithium Batteries. *J. Energy Chem.* **2023**, *86*, 382−390.
(30) Liao, C.; Yu, C.; Peng, L.; Miao, X.; Chen, S.; Zhang, Z.; Cheng, S.; Xie, J. Achieving Superior Ionic Conductivity of Li6PS5I via Introducing LiCl. *Solid State Ionics* **2022**, *377* (January), No. 115871.
(31) Boulineau, S.; Courty, M.; Tarascon, J. M.; Viallet, V. Mechanochemical Synthesis of Li-Argyrodite Li 6PS 5X (X = Cl, Br, I) as Sulfur-Based Solid Electrolytes for All Solid State Batteries Application. *Solid State Ionics* **2012**, *221*, 1−5.
(32) Yang, K.; Dong, J.; Zhang, L.; Li, Y.; Wang, L. Dual Doping: An Effective Method to Enhance the Electrochemical Properties of Li10GeP2S12-Based Solid Electrolytes. *J. Am. Ceram. Soc.* **2015**, *98* (12), 3831−3835.
(33) Arnold, W.; Shreyas, V.; Akter, S.; Li, Y.; Halacoglu, S.; Kalutara Koralalage, M. B.; Guo, X.; Vithanage, D.; Wei, W.; Sumanasekera, G.; Jasinski, J. B.; Narayanan, B.; Wang, H. Highly Conductive Iodine and Fluorine Dual-Doped Argyrodite Solid Electrolyte for Lithium Metal Batteries. *J. Phys. Chem. C* **2023**, *127* (25), 11801−11809.
(34) Yu, T.; Liang, J.; Luo, L.; Wang, L.; Zhao, F.; Xu, G.; Bai, X.; Yang, R.; Zhao, S.; Wang, J.; Yu, J.; Sun, X. Superionic Fluorinated Halide Solid Electrolytes for Highly Stable Li-Metal in All-Solid-State Li Batteries. *Adv. Energy Mater.* **2021**, *11* (36), 1−9.
(35) Ganesan, P.; Soans, M.; Cambaz, M. A.; Zimmermanns, R.; Gond, R.; Fuchs, S.; Hu, Y.; Baumgart, S.; Sotoudeh, M.; Stepien, D.; Stein, H.; Groß, A.; Bresser, D.; Varzi, A.; Fichtner, M. Fluorine-Substituted Halide Solid Electrolytes with Enhanced Stability toward the Lithium Metal. *ACS Appl. Mater. Interfaces* **2023**, *15* (32), 38391−38402.
(36) Ganesan, P.; Zimmermanns, R.; Liang, J.; Hu, Y.; Cuello, G. J.; Puente Orench, I.; Baumgart, S.; Sotoudeh, M.; Groß, A.; Diemant, T.; Varzi, A.; Fichtner, M. In-Depth Analysis of the Origin of Enhanced Ionic Conductivity of Halide-Based Solid-State Electrolyte by Anion Site Substitution. *Batter. Supercaps* **2025**, No. e202500378.
(37) Woodward, P. M. Octahedral Tilting in Perovskites. II. Structure Stabilizing Forces. *Acta Crystallogr. Sect. B Struct. Sci.* **1997**, *53* (1), 44−66.
(38) Yin, J.; Xu, Z.; Hu, Q.; Teobaldi, G.; Liu, L. M.; Prezhdo, O. V. Tuning Octahedral Tilting by Doping to Prevent Detrimental Phase Transition and Extend Carrier Lifetime in Organometallic Perovskites. *J. Am. Chem. Soc.* **2023**, *145* (9), 5393−5399.
(39) López, J. F.; Riós, M.; Mendoza, G. A. Effects of Doping on the Structural Distortion of La0.7Dy0.3Mn1-XZnxO3. *Acta Phys. Polym., A* **2017**, *131* (5), 1254−1255.
(40) Jiang, P.; Neuefeind, J. C.; Avdeev, M.; Huang, Q.; Yue, M.; Yang, X.; Cong, R.; Yang, T. Unprecedented Lattice Volume Expansion on Doping Stereochemically Active Pb2+ into Uniaxially Strained Structure of CaBa1−xPbxZn2Ga2O7. *Nat. Commun.* **2020**, *11* (1), 1−7.
(41) Aso, R.; Kan, D.; Shimakawa, Y.; Kurata, H. Atomic Level Observation of Octahedral Distortions at the Perovskite Oxide Heterointerface. *Sci. Rep.* **2013**, *3*, 1−6.
(42) Huang, H.; Wu, H. H.; Wang, X.; Huang, B.; Zhang, T. Y. Enhancing Sodium Ionic Conductivity in Tetragonal-Na3PS4 by Halogen Doping: A First Principles Investigation. *Phys. Chem. Chem. Phys.* **2018**, *20* (31), 20525−20533.
(43) Yu, L.; Yin, J.; Gao, C.; Lin, C.; Shen, X.; Dai, S.; Jiao, Q. Halogen Doping Mechanism and Interface Strengthening in the Na3SbS4 Electrolyte via Solid-State Synthesis. *ACS Appl. Mater. Interfaces* **2023**, *15* (26), 31635−31642.
(44) Jalem, R.; Gao, B.; Tian, H. K.; Tateyama, Y. Theoretical Study on Stability and Ion Transport Property with Halide Doping of Na3SbS4 Electrolyte for All-Solid-State Batteries. *J. Mater. Chem. A* **2022**, *10* (5), 2235−2248.
(45) Henkelman, G.; Uberuaga, B. P.; Jonsson, H. A Climbing Image Nudged Elastic Band Method for Finding Saddle Points and Minimum Energy Paths. *J. Chem. Phys. 113* **2000**, *113* (22), 9901−9904.
(46) Henkelman, G.; Jónsson, H. Improved Tangent Estimate in the Nudged Elastic Band Method for Finding Minimum Energy Paths and Saddle Points. *J. Chem. Phys.* **2000**, *113* (22), 9978−9985.
(47) Vegard, L. Die Konstitution der Mischkristalle und die Raumffillung der Atome. *J. Mater. Sci.* **1921**, *5* (1), 17−26.
(48) Ravalli, M.; Soleimanzade, M.; Scavini, M.; Tarantino, S. C.; Radaelli, M.; Tealdi, C. Unveiling the Relationship between Polymorphism and Ionic Conductivity in Na3−xSb1−xWxS4 Solid Electrolyte for Na-Ion Batteries. *J. Mater. Chem. A* **2024**, *12*, 31861−31870.
(49) Xiao, R.; Li, H.; Chen, L. High-Throughput Design and Optimization of Fast Lithium Ion Conductors by the Combination of Bond-Valence Method and Density Functional Theory. *Sci. Rep.* **2015**, *5* (June), 1−11.
(50) Hamed, S.; Obrezkov, F.; Huotari, S.; Colalongo, M.; Mousavihashemi, S.; Kallio, T. Optimized NMC622 Electrodes with a High Content of the Active Material: A Comprehensive Study. *J. Power Sources* **2024**, *608* (March), No. 234549.
(51) Yang, J.; Mao, G.; Yao, T.; Shen, L.; Yu, Y. Fluorination from Surface to Bulk Stabilizing High Nickel Cathode Materials with Outstanding Electrochemical Performance. *Angew. Chemie - Int. Ed.* **2025**, *64*, No. e202420413.
(52) Xu, D.; He, J.; He, Y.; Wang, S.; Wu, G.; Li, M.; Cheng, H.; Yu, K.; Huang, X.; Tian, B. Amorphization of Halide Solid Electrolytes for Lithium Super-Ionic Conductivity. *J. Mater. Chem. A* **2024**, *12* (40), 27694−27702.
(53) Chen, Y.; Jin, Y.; Yang, J.; Ren, Y.; Duan, Z.; Liu, X.; Sun, J.; Liu, S.; Zhu, X.; Duan, X. Reply to Comment on "Chemical Vapor Deposition Synthesis and Raman Scattering Investigation of Quasi-One-Dimensional ZrS3 Nanoflakes.". *Nano Res.* **2024**, *17* (9), 8649−8650.
(54) Zhang, Z.; Hu, J.; Hu, Y.; Wang, H.; Hu, H. Lithium Fluorosulfonate-Induced Low-Resistance Interphase Boosting Pouch Batteries Low-Temperature Performance of Commercial Graphite/LiFePO4. *J. Colloid Interface Sci.* **2024**, *669*, 305−313.
(55) Tallman, K. R.; Wheeler, G. P.; Kern, C. J.; Stavitski, E.; Tong, X.; Takeuchi, K. J.; Marschilok, A. C.; Bock, D. C.; Takeuchi, E. S. Nickel-Rich Nickel Manganese Cobalt (NMC622) Cathode Lithiation Mechanism and Extended Cycling Effects Using Operando X-Ray Absorption Spectroscopy. *J. Phys. Chem. C* **2021**, *125* (1), 58−73.
(56) Kondrakov, A. O.; Geßwein, H.; Galdina, K.; De Biasi, L.; Meded, V.; Filatova, E. O.; Schumacher, G.; Wenzel, W.; Hartmann, P.; Brezesinski, T.; Janek, J. Charge-Transfer-Induced Lattice Collapse in Ni-Rich NCM Cathode Materials during Delithiation. *J. Phys. Chem. C* **2017**, *121* (39), 24381−24388.

(57) Tsai, Y. W.; Hwang, B. J.; Ceder, G.; Sheu, H. S.; Liu, D. G.; Lee, J. F. In-Situ X-Ray Absorption Spectroscopic Study on Variation of Electronic Transitions and Local Structure of LiNi 1/3Co 1/3Mn 1/3O 2 Cathode Material during Electrochemical Cycling. *Chem. Mater.* **2005**, *17* (12), 3191−3199.
(58) Koga, H.; Croguennec, L.; Menetrier, M.; Mannessiez, P.; Weill, F.; Delmas, C.; Belin, S. Operando X - Ray Absorption Study of the Redox Processes Involved Li Ion Batteries. *J. Phys. Chem. C* **2014**, *118*, 5700−5709.
(59) Zheng, Y.; Zhang, R.; Vanaphuti, P.; Liu, Y.; Yang, Z.; Wang, Y. Positive Role of Fluorine Impurity in Recovered LiNi0.6Co0.2Mn0.2O2Cathode Materials. *ACS Appl. Mater. Interfaces* **2021**, *13* (48), 57171−57181.
(60) Peralta, D.; Salomon, J.; Reynier, Y.; Martin, J. F.; De Vito, E.; Colin, J. F.; Boulineau, A.; Bourbon, C.; Amestoy, B.; Tisseraud, C.; Pellenc, R.; Ferrandis, J. L.; Bloch, D.; Patoux, S. Influence of Al and F Surface Modifications on the Sudden Death Effect of Si-Gr/Li1.2Ni0.2Mn0.6O2 Li-Ion Cells. *Electrochim. Acta* **2021**, *400*, 139419.
(61) M. Julien, C.; Mauger, A. Functional Behavior of AlF3 Coatings for High-Performance Cathode Materials for Lithium-Ion Batteries. *AIMS Mater. Sci.* **2019**, *6* (3), 406−440.
(62) Wang, K.; Mao, Q.; Lu, X.; Zhang, J.; Huang, H.; Gan, Y.; He, X.; Xia, X.; Zhang, W.; Xia, Y. Fluorides Coated Ni-Rich Cathode Materials with Enhanced Surficial Chemical Stability for Advanced Lithium-Ion Battery. *Sustain. Mater. Technol.* **2023**, *38*, No. e00713.